Article | Open Access

Energy Materials

Roitzheim *et al. Energy Mater.* **2026**, *6*, 600028 **DOI:**10.20517/energymater.2025.174

# Fully inorganic LLZO-based composite cathodes: the impact of Ga substitution on compatibility with cathode active materials during co-sintering

**Christoph Roitzheim[1,*], Franziska Hueppe[2], Yoo Jung Sohn[1], Yannic Collette[1,5], Walter Sebastian Scheld[1], Doris Sebold[1], Thomas Demuth[2], Kerstin Volz[2], Olivier Guillon[1,3,4], Dina Fattakhova-Rohlfing[1,3,5,*], Martin Finsterbusch[1,3]**

**Keywords:**
All-solid-state battery, oxide solid-state electrolyte, LLZO:Ga, LCO, NCM111, NCM811

**Citation:** Roitzheim, C.; Hueppe, F.; Sohn, Y. J.; Collette, Y.; Scheld, W. S.; Sebold, D.; Demuth, T.; Volz, K.; Guillon, O.; Fattakhova-Rohlfing, D.; Finsterbusch, M. Fully inorganic LLZO-based composite cathodes: the impact of Ga substitution on compatibility with cathode active materials during co-sintering. *Energy Mater.* **2026**, *6*, 600028. https://dx.doi.org/10.20517/energymater.2025.174

**Received:** 17 Oct 2025 **First Decision:** 6 Nov 2025 **Revised:** 19 Nov 2025 **Accepted:** 3 Dec 2025 **Published:** 24 Mar 2026

**Academic Editor:** Sen Xin **Copy Editor:** Fangling Lan **Production Editor:** Fangling Lan

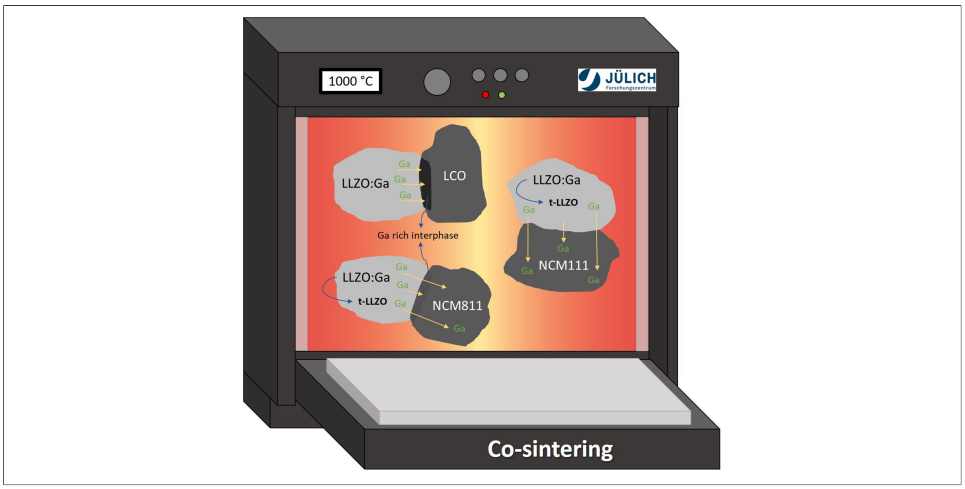


## Abstract

In order to make garnet-based all-solid-state batteries (ASSBs) attractive for industrial applications, their rate capability has to be significantly improved. Recently, cubic $Li_{6.4}Ga_{0.2}La_3Zr_2O_{12}$ (LLZO:Ga) was found to have the highest total ionic conductivity of any oxide solid-state electrolyte by far, reaching up to $2 \times 10^{-3}$ S/cm at room temperature. Since the rate performance of composite cathodes is directly linked to their ionic conductivity, LLZO:Ga is an ideal solid-state electrolyte for high-performance ASSBs. However, careful material selection is required for the fabrication of such ceramic composite cathodes at elevated temperatures in order to avoid incompatibility issues that could lead to low electrochemical performance. We therefore systematically studied the co-sintering behavior of cubic LLZO:Ga in combination with common cathode active materials, including $LiCoO_2$ (LCO), $LiNi_{1/3}Mn_{1/3}Co_{1/3}O_2$ (NCM111), and $LiNi_{0.8}Mn_{0.1}Co_{0.1}O_2$ (NCM811). The analyses were performed using X-ray diffraction, Raman spectroscopy, scanning electron microscopy, and transmission electron microscopy. The experimental conditions were chosen to enable a direct comparison with our previous study on

[1]Institute of Energy Materials and Devices - Materials Synthesis and Processing (IMD-2), Forschungszentrum Jülich GmbH, Jülich 52425, Germany.
[2]Department of Physics and Mar.Quest|Marburg Center for Quantum Materials and Sustainable Technologies, Philipps University Marburg, Marburg 35032, Germany.
[3]Helmholtz Institute Münster, Ionics in Energy Storage (IMD-4), Münster 48149, Germany.
[4]Jülich-Aachen Research Alliance, JARA-Energy, Jülich 52425, Germany.
[5]Faculty of Engineering and Center for Nanointegration Duisburg-Essen (CENIDE), Universität Duisburg-Essen, Duisburg 47057, Germany.

*Correspondence to: Dr. Christoph Roitzheim, Institute of Energy Materials and Devices - Materials Synthesis and Processing (IMD-2), Forschungszentrum Jülich GmbH, Wilhelm Johnen Str., Jülich 52425, Germany. E-mail: c.roitzheim@fz-juelich.de; Prof. Dr. Dina Fattakhova-Rohlfing, Institute of Energy Materials and Devices - Materials Synthesis and Processing (IMD-2), Forschungszentrum Jülich GmbH, Wilhelm Johnen Str., Jülich 52425, Germany. E-mail: d.fattakhova-rohlfing@fz-juelich.de

$Li_{6.45}La_3Zr_{1.6}Ta_{0.4}Al_{0.05}O_{12}$ (LLZO:Ta). For the first time, we were thus able to elucidate the impact of different LLZO compositions on material compatibility. While most of the observed secondary phases were similar to those found for LLZO:Ta-based composites, a more severe degradation of the cubic LLZO:Ga structure itself was observed, reducing its conductivity and thus limiting the performance of the final cell. Consequently, the processing window for producing LLZO:Ga-based composite cathodes is even narrower than for LLZO with other dopants, thus requiring careful tailoring and tight control over the processing conditions when manufacturing garnet-based ASSBs.

## INTRODUCTION

All-solid-state lithium batteries are considered to be promising candidates for next-generation energy storage systems. They offer solutions to several challenges of current lithium-ion battery (LIB) technology, primarily by replacing the flammable organic electrolyte with a solid-state electrolyte (SSE). The SSE can prevent unwanted chemical reactions, resulting in excellent long-term stability. Additionally, their high Li-ion transfer number and low polarization can lead to high power densities. Oxide SSEs enable the use of elemental lithium as an anode, leading to a significant increase in the energy density of all-solid-state batteries (ASSBs) compared to conventional LIBs. At the same time, oxide-based ASSBs offer unsurpassed safety at the cell level, enabling the safe use of lithium-metal anodes even when the formation of dendrites cannot be prevented completely[1-7]. Nevertheless, a large variety of solid electrolytes - such as halides, sulfides, oxides, and polymers - are being investigated, with each individual class exhibiting its own strengths and benefits. To date, no individual solid electrolyte has been able to fulfill all the requirements of an "ideal" SSE. Solid polymer electrolytes offer flexibility and good interfacial contact with the electrodes, but suffer from low ionic conductivities ($< 10^{-4}$ S/cm) and inferior thermal and electrochemical stability. In contrast, inorganic ceramic electrolytes (ICEs) exhibit higher ionic conductivities ($10^{-3}$-$10^{-2}$ S/cm), a broad electrochemical window, and high mechanical strength, but offer poor interfacial contact with the electrodes[7-11]. Among the ICEs, garnet-type $Li_7La_3Zr_2O_{12}$ (LLZO) has attracted considerable attention due to its relatively high ionic conductivity (up to $2 \times 10^{-3}$ S/cm at room temperature), processability in air, non-flammability, broad electrochemical stability window, and high reduction stability when used in combination with lithium metal anodes[11-16]. For high-performance ASSBs, which have a thick composite cathode, the SSE must provide a large contact area with the cathode active material (CAM) and percolating pathways with high total ionic conductivity similar to that of a liquid electrolyte penetrating the porous cathode and wetting CAM particles in conventional cells[17]. The fabrication of LLZO-based composite cathodes always requires a heat treatment (sintering) step at temperatures of around 1,000 °C to achieve proper interface bonding between the CAM and SSE particles, as well as the densification of the electrode[18]. These high sintering temperatures often result in material compatibility issues due to the interdiffusion of cations across the LLZO/CAM interface and/or the formation of undesired secondary phases at the interface. Among the various CAMs used in conventional LIBs, $LiCoO_2$ (LCO) is the only one that is thermodynamically stable in combination with LLZO at temperatures of up to 1,085 °C, while other CAMs - such as $LiMn_2O_4$ (LMO), $LiFePO_4$ (LFP), $LiNi_xCo_yMn_zO_2$ (NCM), and $LiNi_xCo_yAl_zO_2$ (NCA) - react at significantly lower temperatures between 400 and 800 °C[13,17,19-23]. LCO has therefore been the CAM of choice for the few reported fully inorganic garnet-type ASSBs[4,24-28] and composite cathodes[29,30] fabricated by co-sintering. However, LCO has a relatively low specific capacity (140 mAh/g) due to an irreversible phase change below a Li content of $x = 0.5$, which limits the energy density of LCO-based ASSBs[31,32]. For higher energy densities, it is necessary to incorporate higher capacity CAMs such as Ni-rich NCM with capacities > 200 mAh/g[1]. In recent years, several NCM-based, fully inorganic[13,24,33] and polymer-based[34,35] garnet-type

ASSBs with sintered composite cathodes have been demonstrated, but stability issues during co-sintering remain a limiting factor. In our previous research articles, we presented comprehensive studies on the thermal stability of different NCM materials in combination with Ta-substituted LLZO [$Li_{6.45}La_3Zr_{1.6}Ta_{0.4}Al_{0.05}O_{12}$ (LLZO:Ta)] and attempted to identify the most promising NCM composition for co-sintered, garnet-type composite cathodes[13,21]. Based on X-ray diffraction (XRD), Raman spectroscopy, and scanning electron microscopy-energy dispersive X-ray spectroscopy (SEM-EDS), we identified three secondary phases: $La_2Li_{0.5}M_{0.5}O_4$ (M = Ni, Co, Mn), a perovskite phase $LaMO_3$ (M = Ni, Co, Mn), and a $Li_{0.5}M_{0.25}Zr_{0.25}O$ (M = Ni, Co, Mn) rock salt phase[13,21]. Numerous studies have demonstrated that the reported values for the formation onset temperature, as well as the amount and nature of the formed secondary phases, strongly depend on the CAM used, the processing and sintering conditions, and the detection method[13,17,19-21,36,37]. In our study, $LiNi_{0.8}Mn_{0.1}Co_{0.1}O_2$ (NCM811) was unexpectedly found to be a promising CAM for integration into garnet-type composite cathodes, as only small amounts of $La_2Li_{0.5}Ni_{0.5}O_4$ were detected at co-sintering temperatures below 800 °C, forming self-constrained isolated particles. As a result, no highly resistive interfaces were formed, and in combination with the sintering aid $Li_3BO_3$ (LBO), a dense and electrochemically active composite cathode consisting of LLZO:Ta, NCM811, and LBO was successfully manufactured at 750 °C. The resulting fully inorganic ASSB delivered an initial discharge capacity of 120 mAh/g[13]. However, considering the theoretical capacity of NCM811 (200 mAh/g), this corresponds to only 60% capacity utilization, highlighting the continued need for optimization to achieve high-energy-density cells. One possible reason for the low utilization of the cathode may be the relatively thick composite cathode in combination with relatively low effective Li-ion conductivity. The aim is to achieve an effective Li-ion conductivity above $2 \times 10^{-3}$ S/cm in order to realize thick composite cathodes and high charge/discharge rates[4]. The effective Li-ion conductivity can be increased either by increasing the fraction of the solid electrolyte, which is not favored since this would reduce the energy density of the cell, or by increasing the ionic conductivity of the electrolyte itself. Compared to LLZO:Ta, which has a total ionic conductivity of $0.8 \times 10^{-3}$ S/cm at room temperature and is used in the aforementioned NCM811-based ASSB, $Li_{6.4}Ga_{0.2}La_3Zr_2O_{12}$ (LLZO:Ga) demonstrates outstanding total ionic conductivity (up to $2 \times 10^{-3}$ S/cm) at room temperature and is attractive for industrial production, since no excess Li is required during synthesis[13,38,39]. To the best of the authors' knowledge, this is the highest ionic conductivity of all oxide Li-ion conductors. LLZO:Ga is therefore the preferred SSE for thick composite cathodes, enabling garnet-type ASSBs with high energy density and high-rate performance.

In this work, we built on our earlier investigations into the thermal compatibility of different CAMs and LLZO[13,21], using a similar experimental approach, but extended the study to a different LLZO composition with higher ionic conductivity. While we previously only investigated cubic LLZO:Ta as the SSE, we now examine the thermodynamic stability between cubic LLZO:Ga and three different layered CAMs-LCO, $LiNi_{1/3}Mn_{1/3}Co_{1/3}O_2$ (NCM111), and NCM811 - during co-sintering at elevated temperatures of up to 1,000 °C. For comparison purposes, we applied identical co-sintering conditions to those used in our earlier study, in which we investigated CAMs in combination with LLZO:Ta. For the first time, our comprehensive study provides valuable insights into the effects of Ga substitution in LLZO on secondary phase formation during the composite cathode fabrication by co-sintering. It also enables a reliable comparison of the compatibility of three different CAMs with two LLZO compositions, thereby elucidating the impact of the LLZO dopants on side-phase formation. We found that both the CAM and LLZO compositions strongly affect thermal compatibility. For LLZO:Ga, LCO is the most stable CAM, exhibiting the lowest amount of undesired secondary phases and very limited Ga leaching from LLZO, thus reducing the destabilization of the cubic structure. In contrast, we found pronounced Ga leaching and the subsequent formation of tetragonal LLZO (t-LLZO) for NCM. Interestingly, the formation of the detrimental t-LLZO phase was found to be the main difference of using Ga instead of Ta substitution.

## EXPERIMENTAL

The Ga-substituted LLZO (nominal composition: LLZO:Ga) was synthesized via a solid-state reaction (SSR), as previously described[38]. The starting materials $LiOH·H_2O$ (AppliChem GmbH, Darmstadt, Germany, 99%), $La_2O_3$ (Merck Chemicals GmbH, Darmstadt, Germany, 99.9%, 10 h pre-dried at 900 °C), $ZrO_2$ (Treibacher Industrie AG, Althofen, Austria, 99.7%), and $Ga_2O_3$ (Alfa Aesar, Darmstadt, Germany, 99.995%) were weighed in a stoichiometric ratio and homogenized using an automatic mortar grinder (RM 200, Retsch GmbH, Haan, Germany). Pellets were pressed from the homogenized powder (uniaxial, 20 MPa) and calcined twice for 20 h in alumina crucibles using a muffle furnace (LT 5/13, Nabertherm GmbH, Lilienthal, Germany). The first calcination step was performed at 850 °C, and the second one at a higher temperature of 1,000 °C. After each calcination step, the pellets were ground and repressed. The final pellets were uniaxially pressed at 113 MPa. To avoid possible contamination, the pellets were sintered in a powder bed of the same composition in alumina crucibles at 1,175 °C for 10 h in air. Heating and cooling ramps of 5 $K·min^{-1}$ were chosen for the calcination and sintering steps.

For the thermal compatibility tests, the commercial CAMs-LCO, NCM111, or NCM811 - (MTI Corporation, Richmond, CA, USA, battery grade) were mixed with LLZO:Ga at a weight ratio of 1:1 and homogenized using a mortar and pestle. The CAM powders were used as received (D50:~10 µm), while sintered and ground LLZO:Ga powder (D50: ~6 µm) was used. The powder mixtures were pelletized by pressing with a force of 38 kN and a pressing die with a 13 mm diameter (resulting pellet height: ~1.7 mm). The evolution of secondary phases during heating was investigated by *in situ* high temperature XRD (HT-XRD) using an Empyrean diffractometer (Malvern Panalytical Ltd, Malvern, UK) with Cu-$K_\alpha$ radiation. *In situ* measurements were performed in air for isotherms at the following selected temperatures (°C): 25, 100, 200, 300, 350, 400, 450, 500, 550, 600, 650, 700, 750, 800, 900, and 1,000. The heating rate applied to reach the next temperature was 5 K $min^{-1}$. Data were collected over a 2θ range of 10°-80°, with a step width of 0.026° and an accumulation time of 200 s using a 255-channel PIXcel detector, resulting in a holding time of roughly 37 min at each selected temperature during the *in situ* measurement. For further *ex-situ* analysis of the secondary phases formed during co-sintering, two further sets of the aforementioned CAM/LLZO:Ga pellets were prepared. These pellets were sintered on an LLZO:Ga powder bed, which was placed on a MgO plate in an $Al_2O_3$ crucible, at 1,000 °C for 1 h in air at a heating rate of 5 K/min using a muffle furnace (LT 5/13, Nabertherm GmbH, Lilienthal, Germany). One set of the sintered pellets was pulverized using a pestle and mortar for X-ray powder diffraction (XRD). Measurements were carried out using a D4 ENDEAVOR (Bruker Corporation, Billerica, MA, USA) with Cu-$K_\alpha$ radiation. XRD data were collected over a 2θ range of 10°-140°, with a step width of 0.02° and a collection time of 0.75 s/step. Qualitative phase analysis of the diffraction patterns was performed using the powder diffraction file (PDF) database and the inorganic crystal structure database (ICSD) with HighScore software (Malvern Panalytical Ltd, Malvern, UK)[40]. For all of the obtained patterns, crystal structural refinement and the determination of lattice parameters were carried out by Rietveld refinement using Topas V 4.2 software (Bruker Corporation, Billerica, MA, USA)[41].

Further phase analysis was performed by Raman spectroscopy using an inVia™ (Renishaw plc, Wotton-under-Edge, UK) Raman microscope with a 532 nm laser (~2.5 mW) and a 2,400 L $mm^{-1}$ grating. The second set of sintered pellets was analyzed here. The spectra were collected as a map with a step size of 1 µm × 1 µm over an area of 80 µm × 40 µm, resulting in a total of 3,321 spectra, with an acquisition time of 1 s per spectrum at each point. The spectra were processed, including cosmic ray removal and normalization, and the mappings were finally averaged to yield a single spectrum.

For microstructural investigations and secondary phase detection and visualization, scanning electron microscopy (SEM) was performed using a Zeiss Gemini SEM 450 (Carl Zeiss Microscopy Deutschland

GmbH, Oberkochen, Germany) equipped with an Ultim® Max 170 energy-dispersive X-ray spectroscopy (EDS) detector (Oxford Instruments plc, Abingdon, UK). Prior to analysis, the co-sintered pellet samples were embedded in EpoFix epoxy (Struers GmbH, Willich, Germany) and mirror polished. To gain a more detailed understanding of the CAM/LLZO:Ga interface, EDS was performed in a scanning transmission electron microscopy (STEM) with a Bruker Nano XFlash Detector 5060 (Bruker Corporation, Billerica, MA, USA) and the data were evaluated with Esprit 2.3 software. The measurements were carried out in a double Cs-corrected JEOL JEM-2200FS STEM (JEOL Ltd., Akishima, Tokyo, Japan) with an acceleration voltage of 200 kV and a convergence angle of 22.6 mrad. As STEM analysis requires electron-transparent samples (thickness < 100 nm), lamella preparation and Xe-ion beam thinning were carried out in advance using the Helios™ 5 Hydra CX DualBeam (Thermo Fisher Scientific Inc., Waltham, MA, USA). The samples were transferred in an inert gas atmosphere from an argon-filled glovebox ($O_2$ < 0.1 ppm, $H_2O$ < 1 ppm) to the Helios Hydra and back using the Hydra's inert transfer system (CleanConnect). The samples were then loaded into a vacuum transfer TEM holder (Melbuild Corporation, Fukuoka, Japan) to ensure transfer to the microscope without air contamination.

## RESULTS AND DISCUSSION

We first investigated the thermodynamic stability of LLZO:Ga in combination with different CAMs (LCO, NCM111, and NCM811) during co-sintering based on XRD. This approach allowed us to determine the onset temperature of secondary phase formation. To scan a wide temperature range on a single sample, *in situ* high-temperature XRD (HT-XRD) measurements were performed between room temperature and 1,000 °C [Figure 1]. The pyrochlore LLZO phase ($La_2Zr_2O_7$) formed at low co-sintering temperatures of around 500 °C, was present up to 700-800 °C, and disappeared again at higher temperatures, as described previously[13,42,43]. No pyrochlore phase was detected for LCO + LLZO:Ga. It is assumed to have formed, but in an amount below the detection limit of XRD. For all cathode material + LLZO:Ga mixtures, the CAM and LLZO phases were the main phases present in the investigated temperature range. In the case of LCO, no additional secondary phases were observed up to 1,000 °C. It should be noted that the LLZO reflection at ~37° 2θ was no longer observed. A continuous shift to smaller angles, due to lattice expansion during heat treatment, leads to an overlapping of LLZO and LCO reflections in this region of the pattern. For both NCM111- and NCM811-based composites, the first side phases were observed at 700 °C, indicating that the maximum co-sintering temperature without side phase formation is 650 °C for NCM. Additional HT-XRD patterns, which are not shown in Figure 1, are available as Supplementary Figures 1-3. In general, reflections originating from three secondary phases appeared during co-sintering. These were identified as $Li_2ZrO_3$, $La_2(M_{0.5}Li_{0.5})O_4$ (M = Ni, Co), and $LaMO_3$ (M = Ni, Co, Mn) with perovskite structure. While all three phases formed in the case of NCM111, the perovskite phase ($LaMO_3$) did not form for NCM811 + LLZO:Ga. Once formed, the intensity of the reflections originating from this perovskite phase increased steadily with temperature [Figure 1D], while the intensity of $Li_2ZrO_3$ remained almost constant and disappeared completely for NCM811 + LLZO:Ga above 850 °C. The reflection intensity of the $La_2(M_{0.5}Li_{0.5})O_4$ phase initially increased with temperature, then decreased and finally remained constant from 900 °C for NCM811 + LLZO:Ga. For NCM111, $La_2(M_{0.5}Li_{0.5})O_4$ was no longer detected by HT-XRD above 900 °C [Figure 1D]. A summary of the HT-XRD results, indicating the temperature ranges at which the secondary phases appear, is provided in Supplementary Table 1. Based on these initial HT-XRD results, the chemical compatibility between LLZO:Ga and common cathode materials is comparable to that of LLZO:Ta-based composites[13,19]. Besides $Li_2ZrO_3$, which was not found in the case of LLZO:Ta, similar secondary phases were detected in the case of LLZO:Ga. A similar secondary phase evolution was also previously observed by HT-XRD during the co-sintering of NCM and LLZO:Ta[13].

*In situ* HT-XRD is a suitable method for qualitatively studying secondary phase formation during the co-sintering of CAM and LLZO:Ga over a wide temperature range. However, this method only measures the

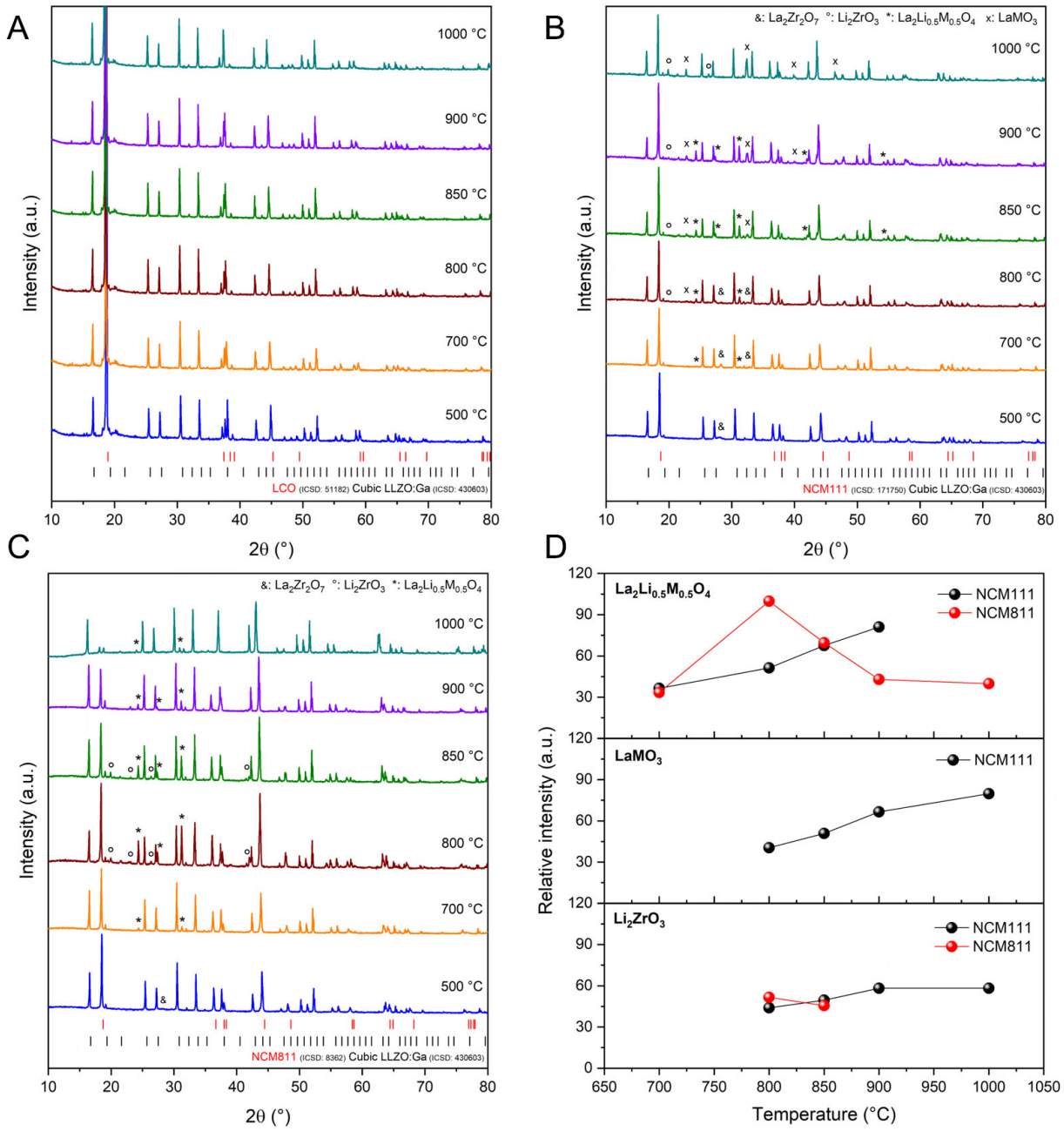


**Figure 1.** *In situ* HT-XRD patterns for 1:1 mixtures of cubic LLZO:Ga with (A) LCO, (B) NCM111, and (C) NCM811. Only selected temperatures are shown. Diffractions attributed to the pyrochlore or secondary phases are labeled accordingly. Due to thermal expansion at elevated temperatures, the Bragg peak positions are shifted slightly in comparison to the reference pattern for LCO, NCM111, NCM811, and cubic LLZO:Ga. (D) Relative intensities of the secondary phase reflections of $Li_2ZrO_3$ (110) at ~19.9° 2θ, $La_2(M_{0.5}Li_{0.5})O_4$ reflection (131) at ~31.3° 2θ, and $LaMO_3$ reflection (121) at ~32.5° 2θ (M = Ni, Co, Mn). All intensities are normalized to the LLZO:Ga reflection (024) at ~30.5° 2θ. Further patterns are available as Supplementary Figures 1-3.

surface of the pellet. To obtain more reliable and precise results that include the bulk of the composite, the same CAM + LLZO:Ga mixtures used for the HT-XRD investigations were sintered at 1,000 °C for 1 h in a conventional muffle furnace. They were then ground and analyzed as a powder by XRD. Figure 2 shows the powder diffractograms of the co-sintered CAM + LLZO:Ga mixtures. Qualitative and quantitative phase analysis was performed based on Rietveld refinement. The refined patterns are shown in the Supplementary Figure 4.

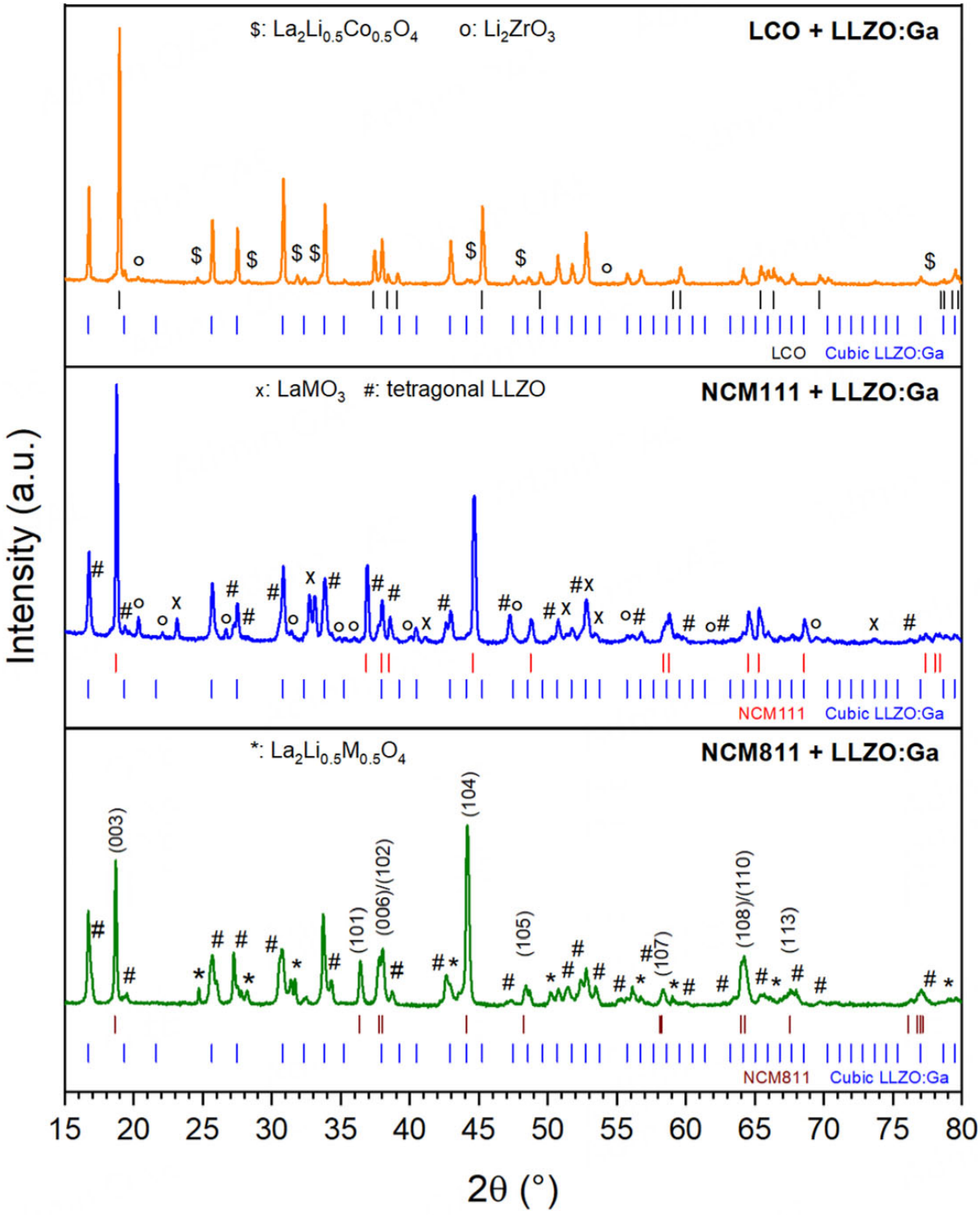


**Figure 2.** Powder XRD patterns of the different CAM + LLZO:Ga mixtures obtained after co-sintering at 1,000 °C using Cu k$\alpha_{1/2}$ radiation. All intensities are normalized to the LLZO:Ga reflection (024) at ~30.8 °2θ. (M = Ni, Co, Mn).

The above-discussed HT-XRD experiments, which mainly analyzed the surface of the composite pellets, led to the conclusion that the LCO + LLZO:Ga mixture is stable during co-sintering. However, a more detailed analysis of the mixture by powder XRD revealed 2 wt.% $La_2(Co_{0.5}Li_{0.5})O_4$ and 3 wt.% $Li_2ZrO_3$ as secondary phases after co-sintering at 1,000 °C. The maximum co-sintering temperature without side phase formation

is therefore below 1,000 °C for LCO. LCO and cubic LLZO:Ga remain the main phases; however, a second cubic LLZO:Ga phase with a slightly larger lattice parameter was found compared to the starting material [Supplementary Tables 2 and 3]. This second cubic phase can be assigned to protonated LLZO:Ga, which forms during handling in an ambient atmosphere, as previously reported[38].

For the NCM111-containing composite, undesired secondary phases formed during co-sintering include 9 wt.% $LaMO_3$ (M = Ni, Co, Mn) with a perovskite structure, 5 wt.% $Li_2ZrO_3$, and 8 wt.% t-LLZO. The Ni-rich NCM811 + LLZO:Ga mixture contains only two side phases after co-sintering, namely 3 wt.% $La_2(M_{0.5}Li_{0.5})O_4$ (M = Ni, Co) and 23 wt.% t-LLZO. A summary of the powder XRD results can be found in Supplementary Table 1. Besides the formation of secondary phases, an alteration of the NCM811 structure itself is indicated by a significant change in the NCM811 Bragg reflection intensity ratio $I(003)/I(104)$ [Supplementary Figure 2] and the lattice parameter ratio $c/a$ [Supplementary Tables 2 and 3]. This shift in Bragg reflection intensity was also observed by HT-XRD [Figure 1C]. These shifts can indicate enhanced cation disorder ($Ni^{2+}$ occupies $Li^+$ sites)[44,45], especially after co-sintering when $c/a$ = 4.93. This increase in cation disorder was further confirmed by Rietveld refinement, which shows a significant increase of the cation disorder from around 4% for pristine NCM811 to 21% after co-sintering with LLZO:Ga. Such anti-site defects are known to deteriorate the electrochemical performance of NCM[46]. The co-sintering experiments were performed in air to ensure that the experimental conditions were comparable to those of earlier studies, enabling the precise study of the effect of different LLZO dopants on the chemical compatibility with CAMs. For battery applications, the firing of Ni-rich NCM should always be performed under pure oxygen flow to prevent the formation of $Ni^{2+}$ occupying Li sites.

Changes in lattice parameters during co-sintering were analyzed based on the $a$ and $c$ parameters, which were calculated from the powder XRD pattern [see Supplementary Tables 2 and 3]. For LCO + LLZO:Ga, the lattice parameters did not change significantly within the error range. In the case of the NCM111-containing mixture, the NCM111 lattice parameters remained similar to those of pristine material, while slightly smaller lattice parameters were observed for cubic LLZO. In contrast to NCM111, the lattice parameters $a$ and $c$ of NCM811 increased significantly, while the lattice parameter $a$ of cubic LLZO remained almost unchanged. The increased lattice parameters for NCM811 after heat treatment in the presence of LLZO:Ga are most likely explained by the doping of the NCM host structure with elements from the SSE, such as Zr, La, or Ga.

In addition to XRD, Raman spectroscopy was used to analyze the composites, as it typically has a lower detection limit for side phases compared to XRD. The Raman spectra of the co-sintered CAM + LLZO:Ga mixtures are shown in Figure 3. By comparing the obtained Raman spectrum for the LCO + LLZO:Ga composite [Figure 3A] with the reference Raman spectra of cubic LLZO:Ga[47] and LCO[48], the observed signals can be assigned to the following vibration modes: La cation vibration at 106 $cm^{-1}$ ($T_{2g}$) and 120 $cm^{-1}$ ($E_g$); broad O-bending modes at 226 $cm^{-1}$ ($T_{2g}$) and 275 $cm^{-1}$ ($A_{1g}$); Li vibrational modes at 357 $cm^{-1}$ ($T_{2g}$) and 406 $cm^{-1}$ ($E_g$ or $T_{2g}$); Zr-O bond stretching at 641 $cm^{-1}$ ($A_{1g}$) for LLZO:Ga and O-Co-O bending at 486 $cm^{-1}$ ($E_g$); and Co-O stretching vibrations at 595 $cm^{-1}$ ($A_{1g}$) for LCO. These results confirm the presence of both LCO and cubic LLZO:Ga after co-sintering. However, the two additional bands found at 157 and 689 $cm^{-1}$, which could not be assigned to LLZO:Ga or LCO, indicate the formation of secondary phases. To identify the chemical composition of these phases, the spectra were compared with relevant Raman spectra reported in the literature [Supplementary Figure 5A]. The band at 157 $cm^{-1}$ clearly indicates the formation of $LaCoO_3$, while the more intense peak at 689 $cm^{-1}$ might originate from $LaCoO_3$ or $La_2(Co_{0.5}Li_{0.5})O_4$. Therefore, based on Raman spectroscopy, the formation of both phases cannot be ruled out. Since $La_2(Co_{0.5}Li_{0.5})O_4$ was also confirmed by XRD, it is assumed that $LaCoO_3$ also forms at a concentration below the detection limit of XRD. Additionally, XRD confirmed the formation of a further secondary phase of $Li_2ZrO_3$. However, comparing the obtained Raman spectra with the reference spectrum of $Li_2ZrO_3$[49] provides no further indication of its presence by Raman spectroscopy [Supplementary Figure 5A].

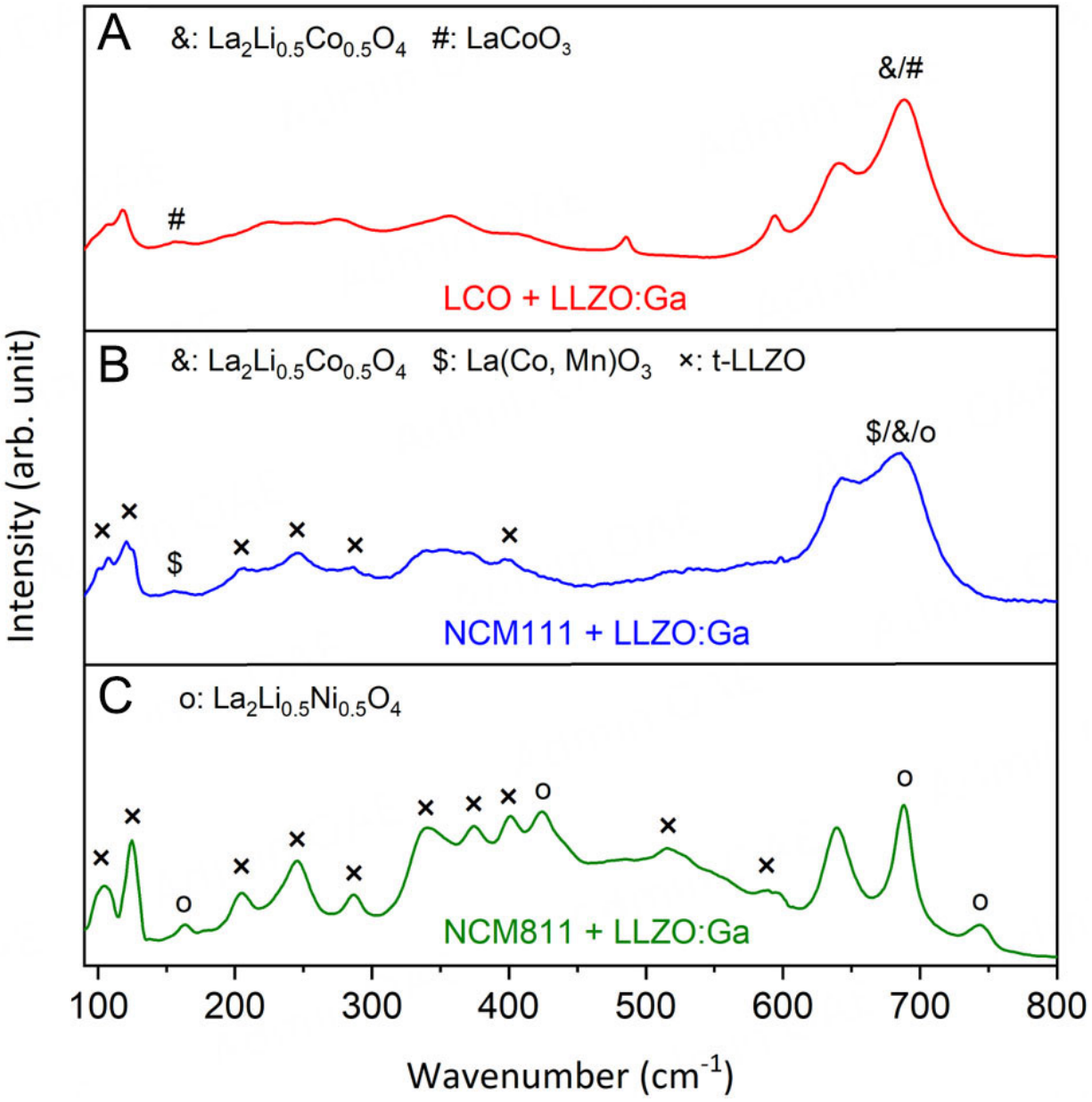


**Figure 3.** Averaged Raman spectra of (A) LCO, (B) NCM111, and (C) NCM811 + LLZO:Ga pellets after co-sintering at 1,000 °C. The signals belonging to secondary phases are labeled accordingly.

In contrast to LCO + LLZO:Ga, where only the cubic LLZO:Ga phase is present after co-sintering at 1,000 °C, the Raman spectra of the NCM111 [Figure 3B] and NCM811 [Figure 3C] composites clearly indicate the presence of the t-LLZO phase, as evidenced by the characteristic bands at 287, 246, and 206 $cm^{-1}$ as well as at 341, 374, and 401 $cm^{-1}$[50]. For NCM111, the split signals at 100, 107, 121 and 126 $cm^{-1}$ further underline the phase transition from cubic to tetragonal[50]. The Raman bands detected at 642 and 639 $cm^{-1}$ for NCM111 and NCM811, respectively, can be attributed to the Zr-O bond stretching (Ref. 639 $cm^{-1}$) ($A_{1g}$) of cubic LLZO:Ga or t-LLZO (Ref. 645 $cm^{-1}$)[50]. The low-intensity bands observed for both NCM-containing samples around 598 $cm^{-1}$ can be attributed to lithiated NCM, which typically exhibits a broad band between 500 and 600 $cm^{-1}$, depending on its transition metal composition[51]. The combination of the two bands at 156

**Table 1. Summary of qualitative and quantitative phase analysis of CAM + LLZO mixtures co-sintered for 1 h at 1,000 °C, based on X-ray diffraction with Rietveld refinement and Raman spectroscopy. Results for LLZO:Ta are from ref.[21]**

| | LLZO:Ta[21] | | LLZO:Ga | |
|---|---|---|---|---|
| | **Secondary phase** | **wt.%** | **Secondary phase** | **wt.%** |
| LCO | * | * | $Li_2ZrO_3$<br>$La_2Li_{0.5}Co_{0.5}O_4$<br>$LaCoO_3$ | 3<br>2<br>- |
| NCM111 | $La_2Li_{0.5}M_{0.5}O_4$<br>$LaMO_3$ | 1<br>0 | $La_2Li_{0.5}M_{0.5}O_4$<br>$Li_2ZrO_3$<br>$LaMO_3$<br>t-LLZO | 0<br>5<br>9<br>8 |
| NCM811 | $La_2Li_{0.5}M_{0.5}O_4$<br>$Li_{0.5}M_{0.25}Zr_{0.25}O$ | 3<br>10 | $La_2Li_{0.5}M_{0.5}O_4$<br>t-LLZO | 3<br>23 |

*LCO was not studied; M = Ni, Co, Mn.

and 686 $cm^{-1}$ is a clear indication of the perovskite phase ($LaMO_3$) formed during the co-sintering of NCM111 + LLZO:Ga [Figure 3B]. A comparison with the reference spectra reveals that M is most likely Co due to the characteristic $LaCoO_3$ band at 687 $cm^{-1}$ (see Supplementary Figure 5B)[52]. A combination with other transition metals, such as $LaCo_{1-x}Mn_xO_3$[19], is also possible. However, $LaMnO_3$[53] and $LaNiO_3$[54] can be excluded due to the absence of bands around 680 $cm^{-1}$ in their Raman spectra. The formation of $La_2(M_{0.5}Li_{0.5})O_4$ in the NCM111-containing mixture cannot be entirely excluded based on Raman spectroscopy, since this phase also exhibits a characteristic band at 686 $cm^{-1}$. However, additional characteristic peaks that would confirm the presence of this phase were not observed (see Supplementary Figure 5B). The Raman peaks observed at 164, 424, 689, and 743 $cm^{-1}$ for the co-sintered NCM811 + LLZO:Ga composite [Figure 3C] can be assigned to $La_2(M_{0.5}Li_{0.5})O_4$. A detailed comparison of the observed Raman shifts with the available reference spectra [Supplementary Figure 5C] suggests that the secondary phase formed in the case of Ni-rich NCM811 is most likely $La_2(Ni_{0.5}Li_{0.5})O_4$. For NCM811, no perovskite phase was formed, as confirmed by Raman spectroscopy and XRD. A summary of the Raman spectroscopy results is available in Supplementary Table 1.

In summary, the XRD and Raman spectroscopy results confirm that cubic LLZO and LCO remained the main phases after the co-sintering of the LCO + LLZO:Ga mixture at 1,000 °C. In total, only around 5 wt.% of side phases ($La_2(Co_{0.5}Li_{0.5})O_4$, $LaCoO_3$, and $Li_2ZrO_3$) were identified based on Rietveld refinement [Table 1]. Our study therefore also indicates reasonably high thermal compatibility between LCO and LLZO:Ga, as is well known for LCO in contact with LLZO[19,23].

Combining LLZO:Ga with CAMs such as NCM, where Co is partially substituted by Ni and Mn, leads to reduced thermodynamic stability, which is in agreement with previous compatibility studies on NCM + LLZO:Ta[13,19,21]. For NCM111 + LLZO:Ga, a total of 22 wt.% secondary phases ($LaMO_3$ (M = Ni, Co, Mn), $Li_2ZrO_3$, and t-LLZO) were identified, while for the Ni-rich NCM811 mixture, an even higher amount of 26 wt.% ($La_2Li_{0.5}M_{0.5}O_4$ (M = Ni, Co, Mn), and t-LLZO) was detected. Table 1 compares the nature and amount of the secondary phases formed for the two different garnet-type SSEs, LLZO:Ga and LLZO:Ta. This direct comparison is possible, since the same CAMs and experimental conditions were used as in our previous work on LLZO:Ta. Therefore, the differences observed here can be directly attributed to the LLZO composition. Unlike LLZO:Ta, $La_2Li_{0.5}M_{0.5}O_4$ was not detected after co-sintering at 1,000 °C for NCM111 + LLZO:Ga. However, it was found to be present at lower temperatures between 700 and 900 °C by HT-XRD. Conversely, the perovskite phase $LaMO_3$ (M = Ni, Co, Mn), which formed in the case of LLZO:Ga, was not detected by XRD for NCM111 + LLZO:Ta co-sintered at 1,000 °C, but was detected at higher temperatures[21]. In the case of NCM811, exactly 3 wt.% $La_2Li_{0.5}M_{0.5}O_4$ (M = Ni, Co, Mn) were detected for

both LLZO compositions. The Zr-containing rock-salt phase ($Li_{0.5}M_{0.25}Zr_{0.25}O$), identified as a secondary phase for NCM811 + LLZO:Ta, was not detected in the case of LLZO:Ga. In this work, $Li_2ZrO_3$ was found to be the Zr-containing phase, with the exception of the NCM811 mixture.

The t-LLZO phase was detected as a detrimental side phase that forms during the co-sintering of NCM + LLZO:Ga, indicating a more intense degradation of the SSE in the case of Ga substitution. For NCM811 in particular, t-LLZO, which exhibits much lower ionic conductivity compared to the cubic phase, forms with a significantly higher weight percentage than the other secondary phases. In general, the tetragonal phase of the garnet increases the ohmic resistance and thus the overpotential during battery cell operation, particularly when located along the CAM/LLZO interface. The possible impact of the other secondary phases on electrochemical performance remains unclear and requires further investigation in follow-up studies.

A phase transition from the cubic to the tetragonal phase during co-sintering was not observed in our previous study on LLZO:Ta-based mixtures, highlighting one of the main issues of using LLZO:Ga instead of LLZO:Ta. Surprisingly, t-LLZO was not observed in the LCO + LLZO:Ga sample, although literature reports that t-LLZO can form at the interface between LLZO and LCO during low-temperature annealing at 700-800 °C[55,56]. Park *et al.*[56] and Ren *et al.*[55] suggested that the leaching of the dopants Al and Ca from LLZO, respectively, might destabilize the cubic structure and promote formation of the t-LLZO phase. To further understand the appearance of the t-LLZO phase in the case of LLZO:Ga and to localize the formed side phases detected by XRD and Raman spectroscopy, microstructural investigations were performed using SEM and STEM in combination with EDS.

Figure 4 shows the cross-sectional SEM images taken with backscattered electrons (BSEs), which visualize the material (Z) contrast, along with the corresponding layered images derived from EDS mappings. The single EDS mappings are available in the supporting information for all of the investigated samples [Supplementary Figures 6-8]. Four regions with different material contrasts can be distinguished for the LCO + LLZO:Ga composite [Figure 4A and B]. In addition to the LLZO (orange) and LCO (blue) main phases, the overlay of the EDS mappings [Figure 4B] and further EDS point analyses [Supplementary Figure 9] confirm the formation of Zr-rich (purple) and La-rich (yellow) secondary phases, which appear as light grey and brighter regions, respectively, in the BSE image. Due to the relatively large excitation volume during EDS analysis and the relatively small regions of side phases, it is not possible to quantify elements or make a valid statement about the secondary phase composition based on EDS. Nevertheless, the SEM/EDS findings support the XRD and Raman spectroscopy results.

For the co-sintered NCM111 + LLZO:Ga mixture, SEM combined with EDS shows very similar side phase formation [Figure 4C and D, Supplementary Figure 10], as was reported for the LCO-containing sample. However, the number of secondary-phase particles is strongly increased compared to the LCO-containing sample. This is consistent with the significantly higher weight fractions of secondary phases found for NCM111 + LLZO:Ga by XRD and Rietveld refinement. Only three regions with different material contrasts could be distinguished for the NCM811 + LLZO:Ga composite [Figure 4E and F], indicating the formation of only one secondary phase with a brighter Z contrast. The EDS spectrum taken from this region, which appears much brighter in the BSE-SEM images and yellow in the EDS mapping, indicates that this particle predominantly contains the elements O, Ni, and La (Li cannot be detected by the EDS detector) [Supplementary Figure 11]. Considering the Raman spectroscopy and XRD results, the bright region observed for the NCM811-containing sample is most likely $La_2Li_{0.5}Ni_{0.5}O_4$, which mainly forms as well-defined, separated particles.

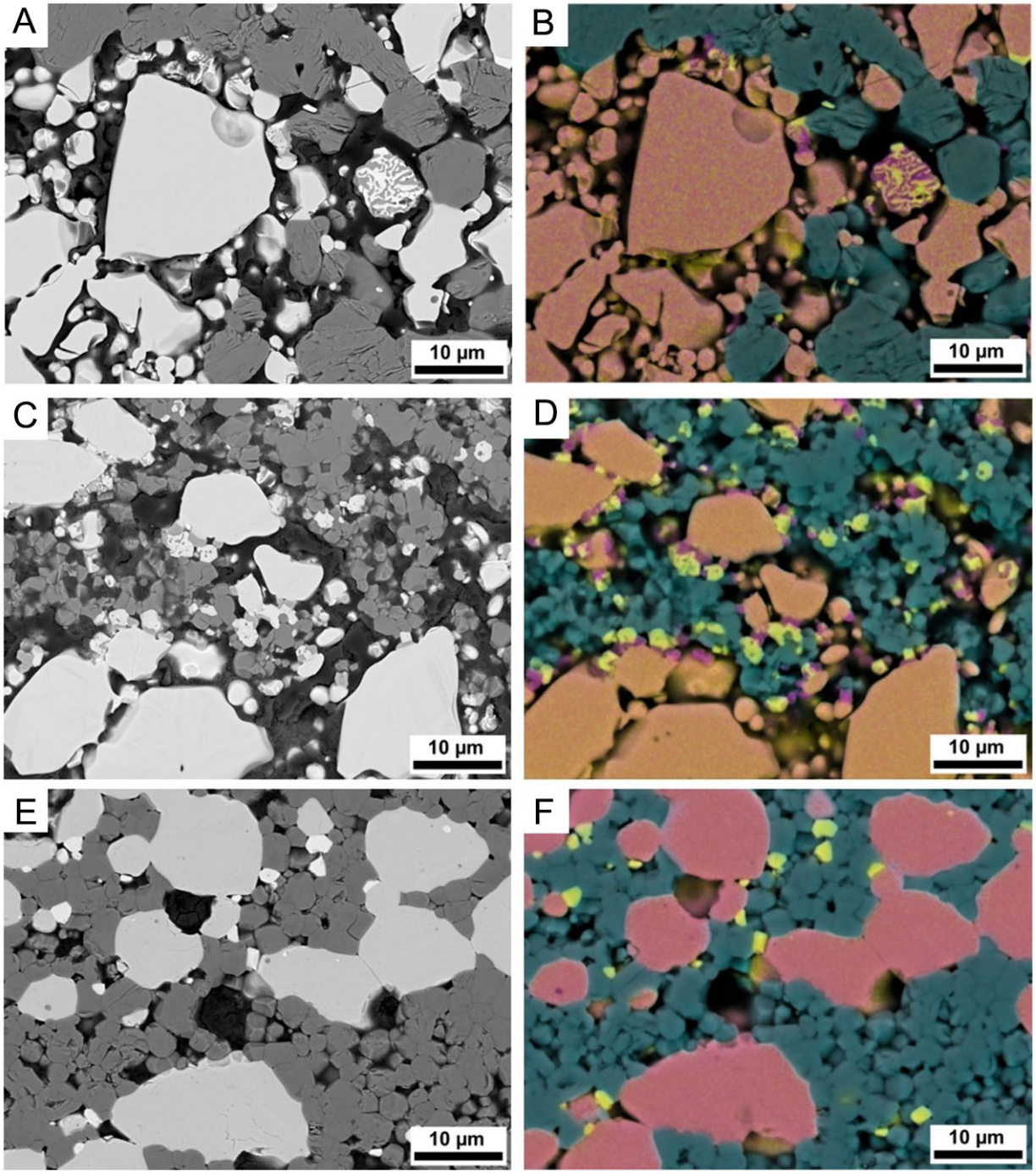


**Figure 4.** Cross-sectional, backscattered electron (BSE) SEM images and the corresponding layered images of the single EDS mappings of La (yellow), Zr (purple), Co (blue), and O (grey) for (A and B) LCO + LLZO:Ga, (C and D) NCM111 + LLZO:Ga, and (E and F) NCM811 + LLZO:Ga after co-sintering at 1,000 °C for 1 h. The complete EDS analysis of these samples is available in the Supplementary Figures 6-8.

None of the characterization methods used thus far have provided reliable insights into the behavior of the element Ga during co-sintering. The Ga mappings [Supplementary Figures 6-8] suggest that Ga is present in both the LLZO and CAM phases after co-sintering at 1,000 °C. However, the overall Ga content is very low and close to the detection limit of the EDS. A more detailed study of Ga distribution after co-sintering, as well as an analysis of the CAM/LLZO:Ga interface, was therefore performed by high-angle annular dark-field (HAADF) imaging and EDS within a STEM. The HAADF-STEM image and EDS analysis of the

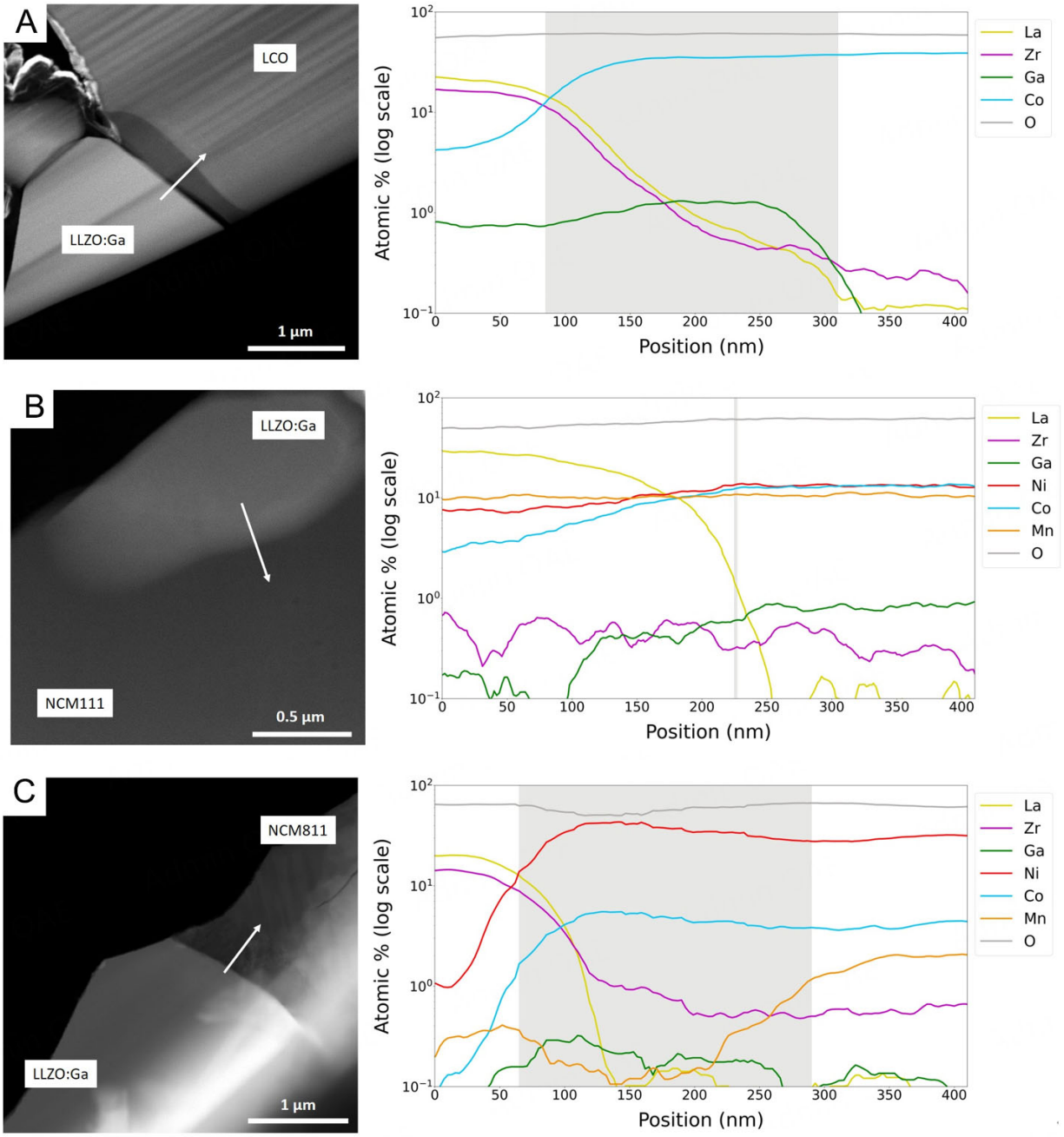


**Figure 5.** HAADF-STEM image (left) and EDS line scan (right) across the interface marked by the arrow for (A) LCO + LLZO:Ga, (B) NCM111 + LLZO:Ga, and (C) NCM811 + LLZO:Ga co-sintered at 1,000 °C. The light grey area in the EDS line scan represents the dark layer at the LCO/LLZO:Ga interface visible in the HAADF image. Further EDS mappings of these samples are available in the Supplementary Figures 12-14.

LCO/LLZO:Ga interface in Figure 5A clearly reveal that a Ga-enriched layer with a different Z contrast (dark grey) formed between the LCO and LLZO:Ga grains (see EDS mapping in Supplementary Figure 12). In this region, the EDS line scan shows a decrease in the La and Zr signals, as well as an initially increasing and subsequently constant Co signal. Diffusion of the elements Zr and La into the LCO structure is only visible at very low concentrations. Furthermore, Ga could not be detected in the LCO bulk.

A different situation was observed at the NCM111/LLZO:Ga interface after co-sintering at 1,000 °C [Figure 5B]. Here, only two phases can be distinguished based on the material contrast in the HAADF-STEM

image and the elemental distribution obtained by EDS analysis (see additional EDS mappings in Supplementary Figure 13). The EDS line scan across the interface region indicates that Ga is depleted in the brighter phase and mainly located in the NCM111 grain. The diffusion of Ni, Co, and Mn from the NCM into the LLZO grain occurred, with Mn exhibiting a near-constant distribution across the interface. Similarly, EDS indicates an almost homogenous Zr distribution in both the LLZO and the NCM111 grains, which is overall very low in the analyzed sample. Due to the significantly lower Zr concentration compared to La, as well as the high Ni, Co, and Mn concentrations in the bright phase, the bright phase observed in this sample is assumed not to be LLZO:Ga, but rather the La-containing side phase identified by XRD and Raman spectroscopy.

In the case of NCM811 + LLZO:Ga, the HAADF-STEM image [Figure 5C] shows a layer with a different Z contrast at the interface, similar to that observed in the LCO+LLZO:Ga sample, although less pronounced. EDS analysis reveals Mn depletion and Ga enrichment in NCM811 at the interface with LLZO:Ga. In contrast to NCM111, only minor diffusion of Ni, Mn, and Co into the LLZO grain is observed in the Ni-rich, NCM811-containing sample [Supplementary Figure 14]. In the case of NCM811, the elements Zr and Ga are also present in the cathode material particles, albeit in very low amounts. La diffusion was not observed for any of the CAM/LLZO:Ga composites. It should be noted that the NCM811 + LLZO:Ga sample also contains Ga-rich phases that do not exhibit significant high concentrations of other transition metals. In contrast to LCO + LLZO:Ga, however, these phases are not located at the CAM/LLZO interface.

The TEM investigations reveal that the dopant Ga, which stabilizes the cubic LLZO structure, is highly mobile during co-sintering with CAMs. The location of Ga after co-sintering strongly depends on the CAM composition in the composite. In the case of LCO, only a Ga-rich, Co-containing interphase forms between the LLZO:Ga and LCO grains; severe Ga diffusion into the LCO bulk does not occur. For the NCM111- and NCM811-containing mixtures, intensive Ga diffusion occurs into the adjacent NCM grain. The few TEM studies on such composite cathodes in the literature used other LLZO compositions, such as LLZO:Ta or $Li_{6.25}Al_{0.25}La_3Zr_2O_{12}$ (LLZO:Al). These studies did not report any Ta or Al diffusion into the CAM grains, nor segregation of LLZO dopants at the CAM/LLZO interface during co-sintering/annealing up to 1,050 °C. Additionally, no phase transition from cubic to tetragonal garnet was reported for their material composition at the investigated co-sintering temperatures. The highly ion-conductive cubic LLZO phase was thus largely maintained after firing[20,28]. Only Park *et al.*[56] observed the formation of t-LLZO when synthesizing and annealing LCO on top of an LLZO layer at 700 °C. They confirmed the partial phase transition at the LLZO/LCO interface by TEM and attributed it to the destabilization of the cubic garnet framework caused by Al leaching from the LLZO and its diffusion into the LCO phase[56]. Based on the interpretation of the work of Park *et al.*[56] by Ren *et al.*[55], the tetragonal phase was caused by LCO leaching Al out of the cubic garnet phase. In their own work, Ren *et al.*[55] annealed an LCO film that was applied by radio frequency sputtering onto Ca- and Ta-substituted LLZO ($Li_7La_{2.75}Ca_{0.25}Zr_{1.75}Ta_{0.25}O_{12}$). They also observed the t-LLZO phase and Ca diffusion into the LCO film after annealing at 800 °C[55]. Based on these previous observations, we assume that in the case of Ga-substituted LLZO, the enhanced mobility of the dopant Ga at elevated temperatures causes Ga loss from the cubic LLZO lattice. This destabilizes the cubic LLZO structure, leading to a partial phase transition from the cubic to the tetragonal phase, as confirmed by XRD and Raman spectroscopy for the NCM111- and NCM811-containing samples after co-sintering. Schwab *et al.*[38] previously observed such a phase shift to t-LLZO by increasing the amount of excess lithium during the synthesis of LLZO:Ga. The thermodynamically more stable t-LLZO phase contains more lithium than the cubic LLZO:Ga phase, which could explain the driving force toward the tetragonal phase in the presence of an additional Li source[38]. In the case of the CAM + LLZO:Ga mixtures investigated in this work, the CAMs can serve as a Li source, since their Li concentration is significantly higher (LCO:31 Li-atoms/nm$^3$; NCM111:30 Li-atoms/nm$^3$; NCM811:29 Li-atoms/nm$^3$) than that of cubic LLZO:Ga (23 Li-atoms/nm$^3$). The

calculation of Li concentrations is provided in the Supplementary Table 4.

A thermodynamically favored Ga incorporation into the CAM host structure would explain an additional driving force for the Ga loss from LLZO and the formation of t-LLZO. Ga-doped LCO[57] and Ga-doped, Ni-rich NCM[58] are well-known in the literature due to their improved electrochemical performance through Ga doping. Ga-doped CAMs are characterized by their high Ga-oxygen bond energies within the layered structure, as evidenced by experimental findings and *ab initio* calculations[57,58]. These higher bond energies are a possible driving force for the incorporation of Ga from the cubic LLZO into the layered structure of the CAMs. Our TEM findings indicate that Ga loss from the LLZO lattice and its subsequent incorporation into the NCM lattice is more preferential than into the LCO lattice. This is underlined by the XRD results, which show a high quantity of t-LLZO and enlarged lattice parameters, especially for NCM811 + LLZO:Ga. This is consistent with the findings of Jamil *et al.*[58] for Ga-doped, Ni-rich NCM. For the NCM811 sample investigated here, Ga doping is the most likely reason for the lattice parameter change after co-sintering, since no significant diffusion of other transition metals was observed by TEM/EDS. The incorporation of $Ga^{3+}$ into the NCM lattice induces positive charges that can be compensated by a partial reduction of $Ni^{3+}$ to $Ni^{2+}$, which can occupy the Li sites and result in increased cation disorder, as determined by Rietveld refinement for NCM811 + LLZO:Ga after co-sintering. For LCO + LLZO:Ga, Ga loss from LLZO, its incorporation into the layered structure, and the formation of t-LLZO were found to be inhibited, since only a Ga-enriched interphase was observed. It is assumed that a small amount of t-LLZO was formed, below the detection limit of the characterization methods used here. It was not possible to distinguish LLZO:Ga from t-LLZO in STEM diffraction mode due to the presence of numerous diffraction spots that could not be unambiguously assigned, likely caused by the coexistence of multiple phases. Based on the present study, the exact reason for the distinct behavior of the LCO/LLZO:Ga composite remains unclear. However, it seems that the Ga-enriched, Co-depleted phase formed at the LLZO/LCO interface blocks further Ga diffusion into the LCO bulk. This allows the cubic LLZO phase to mostly remain intact during co-sintering. Nevertheless, such an interphase can cause very high interfacial resistance, which limits the electrochemical performance of a battery cell.

Based on our study, LCO - which is known to be very stable in contact with LLZO:Ta - is also the most promising CAM that can potentially be co-sintered with LLZO:Ga to fabricate dense composite cathodes for integration into ASSBs. We therefore fabricated fully inorganic cells based on the recipe[4] developed in our group using LCO but LLZO:Ga as the catholyte and solid separator, respectively. The electrochemical performance of the resulting cells was strongly limited due to very high total cell resistance (> 2,000 Ω), resulting in huge ohmic losses during cycling and a discharge capacity of only 42 mAh/g (0.4 mAh/cm$^2$) in the first cycle [Supplementary Figure 15]. The observed Ga-rich interphase is one explanation for the high cell resistance. In addition, cobalt diffusion into the LLZO separator[59] was much more severe and challenging for the Ga-substituted LLZO system. Analysis of the failure mechanism of the LLZO:Ga-based full cells, as well as a detailed study of the transition metal diffusion into the LLZO:Ga separator during half-cell manufacturing by co-sintering, will be addressed in a comprehensive follow-up study.

## CONCLUSION

The thermodynamic stability between the garnet-type SSE LLZO:Ga and three different CAMs - LCO, NCM111, and NCM811 - was investigated in detail and compared to LLZO:Ta. Regardless of the CAM used, the cubic LLZO phase and the initial CAM phase were largely preserved after co-sintering at temperatures up to 1,000 °C. However, various secondary phases were observed close to the CAM/LLZO interface, with their nature, amount, and reaction onset temperature strongly dependent on the chemical composition of the CAM. Four secondary phases - $Li_2ZrO_3$, $La_2Li_{0.5}M_{0.5}O_4$ (M = Ni, Co, Mn), a perovskite phase $LaMO_3$ (M = Ni, Co, Mn), and t-LLZO - were identified based on XRD and Raman spectroscopy. For LCO + LLZO:Ga, only

around 5 wt.% of the secondary phases $Li_2ZrO_3$, $La_2Li_{0.5}Co_{0.5}O_4$, and $LaCoO_3$ formed in total. A Ga-enriched, Co-containing phase was found at the LCO/LLZO:Ga interface by STEM, although extensive Ga diffusion into the LCO bulk and the formation of t-LLZO were not observed. During the high-temperature experiments, 5 wt.% $Li_2ZrO_3$, 9 wt.% $LaCo_{1-x}Mn_xO_3$, and 8 wt.% t-LLZO formed for NCM111 + LLZO:Ga. In contrast to LCO, Ga diffuses extensively into the NCM111 particles, resulting in Ga being primarily located in the NCM phase. In addition, a homogenous Zr distribution and the diffusion of transition metals (mainly Mn) into LLZO were observed. For NCM811 + LLZO:Ga, only two secondary phases formed: 3 wt.% $La_2Li_{0.5}Ni_{0.5}O_4$ and 23 wt.% t-LLZO. Similar to LCO, a Ga-enriched interlayer was detected at the NCM811/LLZO:Ga interface by STEM/EDS; in the case of NCM811, this interlayer was depleted in Mn. As with NCM111, Ga was also detected within the NCM811 bulk. Compared with our previous compatibility study on LLZO:Ta, the LLZO:Ga-containing mixtures behave similarly with respect to the formation of La-containing side phases ($La_2Li_{0.5}M_{0.5}O_4$ (M = Ni, Co, Mn) and $LaMO_3$ (M = Ni, Co, Mn)). NCM811 is the more stable NCM composition when combined with both LLZO:Ta and LLZO:Ga. However, the formation of t-LLZO was the main difference when using Ga-substituted LLZO and had not been previously observed for LLZO:Ta. The formation of t-LLZO was attributed to Ga leaching from the LLZO in the presence of a Li source and subsequent incorporation into the NCM structure. The higher thermodynamic stability of t-LLZO and the higher Ga-oxygen bond energies in the layered structure are possible driving forces for the observed phase transition.

In conclusion, our previous and present studies together demonstrate that both the SSE and CAM composition have a significant impact on chemical stability during the high-temperature fabrication steps required for ASSB manufacturing. Interestingly, the choice of dopant for the LLZO SSE was found to have a more significant impact on material compatibility. LLZO:Ga exhibits the highest ionic conductivity of all the oxide solid-state Li-ion conductors. However, this advantage comes at the price of decreased interface stability due to dopant leaching. The observed phase transformation from cubic to tetragonal must therefore be suppressed during component manufacturing, as the tetragonal phase has significantly lower total ionic conductivity than LLZO:Ga. Therefore, in order to successfully integrate highly conductive LLZO:Ga into co-sintered composite cathodes, strategies must be developed to stabilize the Ga dopant in the LLZO structure during co-sintering at temperatures around 1,000 °C. Two approaches appear to be the most effective in achieving this goal. First, interface engineering via coating of the CAM or SSE with materials that exhibit low Ga incorporation, or the use of sintering aids that modify the interface during high-temperature treatment could suppress Ga leaching from the LLZO:Ga. However, additives used for liquid phase sintering, such as LBO - which has previously been applied successfully in the fabrication of fully inorganic cells[13,33,34] - should be approached with caution in the case of LLZO:Ga, since LBO may also serve as a source of Li and promote the phase shift from cubic to tetragonal. Second, innovative sintering techniques that reduce the interaction time at elevated temperatures, or allow processing at significantly lower temperatures - such as rapid thermal processing (RTP)[60,61], ultra-fast high-temperature sintering (UHS)[62], laser sintering[61,63,64], field-assisted sintering (FAST/SPS)[28,65], or cold sintering[66,67] - could be promising strategies for kinetically limiting secondary phase formation and Ga leaching. These techniques also offer substantial energy savings, further increasing the attractiveness of garnet-based ASSBs for industrial applications.

## DECLARATIONS

### Acknowledgments

The authors would like to thank Christian Dellen (evaluation of Raman spectra), Christian Schwab (calculation of Li-concentrations), Volker Bader (heat treatments), and Philipp Hecker (heat treatments and lab assistance) for their contributions.

### Authors' contributions

Performed the co-sintering experiments, analyzed the data, and wrote the original draft of the manuscript with input from all authors: Roitzheim, C.

Conducted HT-XRD measurements and performed the Rietveld refinements: Sohn, Y. J.
Carried out the TEM investigations: Hueppe, F.; Demuth, T.; Volz, K.
Performed the Raman analysis: Scheld, W. S.
Acquired the SEM images and performed the EDS analysis: Sebold, D.
The manuscript was revised and edited: Roitzheim, C.; Sohn, Y. J.; Hueppe, F.; Demuth, T.; Scheld, W. S.; Collette, Y.; Sebold, D.; Finsterbusch, M.; Fattakhova-Rohlfing, D.; Guillon, O.
Conceived the study, provided the resources, and supervised the work: Finsterbusch, M.; Guillon, O.; Fattakhova-Rohlfing, D.
All authors approved the final version of the manuscript.

## Availability of data and materials

The data supporting the findings of this study (including detailed representations of SEM/EDS and TEM/EDS analyses, Raman spectroscopy data, and results of the Rietveld refinement) can be found in the Supplementary Materials published with this article.

## AI and AI-assisted tools statement

Not applicable.

## Financial support and sponsorship

The authors are grateful for financial support provided by the German Federal Ministry of Research, Technology, and Space (Bundesministerium für Forschung, Technologie und Raumfahrt, BMFTR) under grant numbers 13XP0434A (FB2-Oxid), 03XP0433D (FB2-Char), and 13XP0510A (CatSE2), as well as by the German Research Foundation (Deutsche Forschungsgemeinschaft, DFG) under grant number 429409150 (project E-TIP).

## Conflicts of interest

All authors declared that there are no conflicts of interest.

## Ethical approval and consent to participate

Not applicable.

## Consent for publication

Not applicable.



## Supplementary Materials

Supplementary Materials

## REFERENCES

1. Noh, H.; Youn, S.; Yoon, C. S.; Sun, Y. Comparison of the structural and electrochemical properties of layered $Li[Ni_xCo_yMn_z]O_2$ (x = 1/3, 0.5, 0.6, 0.7, 0.8 and 0.85) cathode material for lithium-ion batteries. *J. Power. Sources.* **2013**, *233*, 121-30. DOI
2. Yao, X.; Huang, B.; Yin, J.; et al. All-solid-state lithium batteries with inorganic solid electrolytes: Review of fundamental science. *Chinese. Phys. B.* **2016**, *25*, 018802. DOI
3. Sakuda, A. Favorable composite electrodes for all-solid-state batteries. *J. Ceram. Soc. Jpn.* **2018**, *126*, 675-83. DOI
4. Finsterbusch, M.; Danner, T.; Tsai, C. L.; Uhlenbruck, S.; Latz, A.; Guillon, O. High capacity garnet-based all-solid-state lithium batteries: fabrication and 3D-microstructure resolved modeling. *ACS. Appl. Mater. Interfaces.* **2018**, *10*, 22329-39. DOI PubMed
5. Janek, J.; Zeier, W. G. A solid future for battery development. *Nat. Energy.* **2016**, *1*, 16141. DOI
6. Janek, J.; Zeier, W. G. Challenges in speeding up solid-state battery development. *Nat. Energy.* **2023**, *8*, 230-40. DOI
7. Schmaltz, T.; Hartmann, F.; Wicke, T.; Weymann, L.; Neef, C.; Janek, J. A roadmap for solid-state batteries. *Adv. Energy. Mater.* **2023**, *13*, 2301886. DOI

8. Thangadurai, V.; Narayanan, S.; Pinzaru, D. Garnet-type solid-state fast Li ion conductors for Li batteries: critical review. *Chem. Soc. Rev.* **2014**, *43*, 4714-27. DOI PubMed
9. Sand, S. C.; Rupp, J. L. M.; Yildiz, B. A critical review on Li-ion transport, chemistry and structure of ceramic-polymer composite electrolytes for solid state batteries. *Chem. Soc. Rev.* **2025**, *54*, 178-200. DOI
10. Xue, Z.; He, D.; Xie, X. Poly(ethylene oxide)-based electrolytes for lithium-ion batteries. *J. Mater. Chem. A.* **2015**, *3*, 19218-53. DOI
11. Li, S.; Zhang, S. Q.; Shen, L.; et al. Progress and perspective of ceramic/polymer composite solid electrolytes for lithium batteries. *Adv. Sci.* **2020**, *7*, 1903088. DOI PubMed PMC
12. Chen, L.; Li, Y.; Li, S.; Fan, L.; Nan, C.; Goodenough, J. B. PEO/garnet composite electrolytes for solid-state lithium batteries: From "ceramic-in-polymer" to "polymer-in-ceramic". *Nano. Energy.* **2018**, *46*, 176-84. DOI
13. Roitzheim, C.; Sohn, Y. J.; Kuo, L.; et al. All-solid-state Li batteries with NCM-garnet-based composite cathodes: the impact of NCM composition on material compatibility. *ACS. Appl. Energy. Mater.* **2022**, *5*, 6913-26. DOI
14. Murugan, R.; Thangadurai, V.; Weppner, W. Fast lithium ion conduction in garnet-type $Li_7La_3Zr_2O_{12}$. *Angew. Chem. Int. Ed.* **2007**, *46*, 7778-81. DOI PubMed
15. Buschmann, H.; Dölle, J.; Berendts, S.; et al. Structure and dynamics of the fast lithium ion conductor "$Li_7La_3Zr_2O_{12}$". *Phys. Chem. Chem. Phys.* **2011**, *13*, 19378-92. DOI
16. Buannic, L.; Orayech, B.; López, Del. Amo. J.; et al. Dual substitution strategy to enhance $Li^+$ ionic conductivity in $Li_7La_3Zr_2O_{12}$ solid electrolyte. *Chem. Mater.* **2017**, *29*, 1769-78. DOI
17. Ren, Y.; Danner, T.; Moy, A.; et al. Oxide-based solid-state batteries: a perspective on composite cathode architecture. *Adv. Energy. Mater.* **2022**, *13*, 2201939. DOI
18. Xiao, Y.; Wang, Y.; Bo, S.; Kim, J. C.; Miara, L. J.; Ceder, G. Understanding interface stability in solid-state batteries. *Nat. Rev. Mater.* **2019**, *5*, 105-26. DOI
19. Ren, Y.; Liu, T.; Shen, Y.; Lin, Y.; Nan, C. Chemical compatibility between garnet-like solid state electrolyte $Li_{6.75}La_3Zr_{1.75}Ta_{0.25}O_{12}$ and major commercial lithium battery cathode materials. *J. Materiomics.* **2016**, *2*, 256-64. DOI
20. Demuth, T.; Fuchs, T.; Walther, F.; et al. Influence of the sintering temperature on LLZO-NCM cathode composites for solid-state batteries studied by transmission electron microscopy. *Matter* **2023**, *6*, 2324-39. DOI
21. Bauer, A.; Roitzheim, C.; Lobe, S.; et al. Impact of Ni-Mn-Co-Al-based cathode material composition on the sintering with garnet solid electrolytes for all-solid-state batteries. *Chem. Mater.* **2023**, *35*, 8958-68. DOI
22. Wakasugi, J.; Munakata, H.; Kanamura, K. Thermal stability of various cathode materials against $Li_{6.25}Al_{0.25}La_3Zr_2O_{12}$ electrolyte. *Electrochemistry* **2017**, *85*, 77-81. DOI
23. Miara, L. J.; Richards, W. D.; Wang, Y. E.; Ceder, G. First-principles studies on cation dopants and electrolyte|cathode interphases for lithium garnets. *Chem. Mater.* **2015**, *27*, 4040-7. DOI
24. Han, S.; Kil, D.; Lee, S.; et al. A full oxide-based solid-state lithium battery and its unexpected cathode degradation mechanism. *ACS. Energy. Lett.* **2023**, *8*, 4794-805. DOI
25. Han, F.; Yue, J.; Chen, C.; et al. Interphase engineering enabled all-ceramic lithium battery. *Joule* **2018**, *2*, 497-508. DOI
26. Ohta, S.; Komagata, S.; Seki, J.; Saeki, T.; Morishita, S.; Asaoka, T. All-solid-state lithium ion battery using garnet-type oxide and $Li_3BO_3$ solid electrolytes fabricated by screen-printing. *J. Power. Sources.* **2013**, *238*, 53-6. DOI
27. Liu, T.; Ren, Y.; Shen, Y.; Zhao, S.; Lin, Y.; Nan, C. Achieving high capacity in bulk-type solid-state lithium ion battery based on $Li_{6.75}La_3Zr_{1.75}Ta_{0.25}O_{12}$ electrolyte: interfacial resistance. *J. Power. Sources.* **2016**, *324*, 349-57. DOI
28. Ihrig, M.; Finsterbusch, M.; Laptev, A. M.; et al. Study of $LiCoO_2$/$Li_7La_3Zr_2O_{12}$:Ta interface degradation in all-solid-state lithium batteries. *ACS. Appl. Mater. Interfaces.* **2022**, *14*, 11288-99. DOI
29. Zhao, H.; Mo, H.; Mao, P.; Ran, R.; Zhou, W.; Liao, K. Tape-casting fabrication techniques for garnet-based membranes in solid-state lithium-metal batteries: a comprehensive review. *ACS. Appl. Mater. Interfaces.* **2024**, *16*, 68772-93. DOI
30. Weinmann, S.; Gobena, H.; Quincke, L.; et al. Stabilizing interfaces of all-ceramic composite cathodes for Li-garnet batteries. *Adv. Energy. Mater.* **2025**, *15*, 2502280. DOI
31. Li, J.; Lin, C.; Weng, M.; et al. Structural origin of the high-voltage instability of lithium cobalt oxide. *Nat. Nanotechnol.* **2021**, *16*, 599-605. DOI
32. Oh, P.; Yun, J.; Choi, J. H.; et al. New ion substitution method to enhance electrochemical reversibility of Co-rich layered materials for Li-ion batteries. *Adv. Energy. Mater.* **2022**, *13*, 2202237. DOI
33. Yin, X.; Li, D.; Hao, L.; et al. A high-energy all-solid-state lithium metal battery with "single-crystal" lithium-rich layered oxides. *Chem. Commun.* **2023**, *59*, 639-42. DOI
34. Wang, D.; Sun, Q.; Luo, J.; et al. Mitigating the interfacial degradation in cathodes for high-performance oxide-based solid-state lithium batteries. *ACS. Appl. Mater. Interfaces.* **2019**, *11*, 4954-61. DOI

35. Hayashi, N.; Watanabe, K. Reaction suppression between a high-Ni cathode material (NMC622) and $Li_7La_3Zr_2O_{12}$ on co-sintering for manufacturing bulk-type all-solid-state batteries: a new method and its mechanism. *Adv. Sci.* **2025**, *12*, e12219. DOI PubMed PMC
36. Ma, Z.; Labriola, G.; Salazar, K. A.; Mi, C. C.; Kong, L. Thermal stability and electrochemical behavior of commercial polycrystalline and single-crystalline cathodes integrated with cubic $Li_{6.4}La_3Zr_{1.4}Ta_{0.6}O_{12}$ for all-solid-state lithium batteries. *J. Mater. Chem. A.* **2025**, *13*, 26647-59. DOI
37. Kim, Y.; Waluyo, I.; Hunt, A.; Yildiz, B. Avoiding $CO_2$ Improves thermal stability at the interface of $Li_7La_3Zr_2O_{12}$ electrolyte with layered oxide cathodes. *Adv. Energy. Mater.* **2022**, *12*, 2102741. DOI
38. Schwab, C.; Häuschen, G.; Mann, M.; et al. Towards economic processing of high performance garnets - case study on zero Li excess Ga-substituted LLZO. *J. Mater. Chem. A.* **2023**, *11*, 5670-80. DOI
39. Qin, S.; Zhu, X.; Jiang, Y.; Ling, M.; Hu, Z.; Zhu, J. Growth of self-textured $Ga^{3+}$-substituted $Li_7La_3Zr_2O_{12}$ ceramics by solid state reaction and their significant enhancement in ionic conductivity. *Appl. Phys. Lett.* **2018**, *112*, 113901. DOI
40. Degen, T.; Sadki, M.; Bron, E.; König, U.; Nénert, G. The HighScore suite. *Powder. Diffr.* **2014**, *29 Suppl*, S13-8. DOI
41. Bruker AXS. Topas V4: General profile and structure analysis software for powder diffraction data. Karlsruhe, Germany; 2008.
42. Larraz, G.; Orera, A.; Sanjuán, M. L. Cubic phases of garnet-type $Li_7La_3Zr_2O_{12}$: the role of hydration. *J. Mater. Chem. A.* **2013**, *1*, 11419. DOI
43. Matsui, M.; Sakamoto, K.; Takahashi, K.; et al. Phase transformation of the garnet structured lithium ion conductor: $Li_7La_3Zr_2O_{12}$. *Solid. State. Ion.* **2014**, *262*, 155-9. DOI
44. Choi, Y. Effects of cation mixing on the electrochemical lithium intercalation reaction into porous $Li_{1-\delta}Ni_{1-y}Co_yO_2$ electrodes. *Solid. State. Ion.* **1996**, *89*, 43-52. DOI
45. Hua, W.; Schwarz, B.; Knapp, M.; et al. (De)Lithiation mechanism of hierarchically layered $LiNi_{1/3}Co_{1/3}Mn_{1/3}O_2$ cathodes during high-voltage cycling. *J. Electrochem. Soc.* **2018**, *166*, A5025-32. DOI
46. Sun, G.; Yin, X.; Yang, W.; et al. The effect of cation mixing controlled by thermal treatment duration on the electrochemical stability of lithium transition-metal oxides. *Phys. Chem. Chem. Phys.* **2017**, *19*, 29886-94. DOI
47. Scheld, W. S.; Collette, Y.; Schwab, C.; et al. Ga-ion migration during co-sintering of heterogeneous Ta- and Ga-substituted LLZO solid-state electrolytes. *J. Eur. Ceram. Soc.* **2025**, *45*, 116936. DOI
48. Gross, T.; Hess, C. Raman diagnostics of $LiCoO_2$ electrodes for lithium-ion batteries. *J. Power. Sources.* **2014**, *256*, 220-5. DOI
49. Yuan, K.; Jin, X.; Xu, C.; et al. Fabrication of dense and porous $Li_2ZrO_3$ nanofibers with electrospinning method. *Appl. Phys. A.* **2018**, *124*, 403. DOI
50. Tietz, F.; Wegener, T.; Gerhards, M.; Giarola, M.; Mariotto, G. Synthesis and Raman micro-spectroscopy investigation of $Li_7La_3Zr_2O_{12}$. *Solid. State. Ion.* **2013**, *230*, 77-82. DOI
51. Flores, E.; Novák, P.; Aschauer, U.; Berg, E. J. Cation ordering and redox chemistry of layered Ni-rich $Li_xNi_{1-2y}Co_yMnyO_2$: an operando Raman spectroscopy study. *Chem. Mater.* **2019**, *32*, 186-94. DOI
52. Gnezdilov, V.; Fomin, V.; Yeremenko, A. V.; et al. Low-temperature mixed spin state of $Co^{3+}$ in $LaCoO_3$ evidenced from Jahn-Teller lattice distortions. *Low. Temp. Phys.* **2006**, *32*, 162-8. DOI
53. Abrashev, M. V.; Litvinchuk, A. P.; Iliev, M. N.; et al. Comparative study of optical phonons in the rhombohedrally distorted perovskites$LaAlO_3$ and $LaMnO_3$. *Phys. Rev. B.* **1999**, *59*, 4146-53. DOI
54. Chaban, N.; Weber, M.; Pignard, S.; Kreisel, J. Phonon Raman scattering of perovskite $LaNiO_3$ thin films. *Appl. Phys. Lett.* **2010**, *97*, 031915. DOI
55. Ren, Y.; Wachsman, E. D. All solid-state Li/LLZO/LCO battery enabled by alumina interfacial coating. *J. Electrochem. Soc.* **2022**, *169*, 040529. DOI
56. Park, K.; Yu, B.; Jung, J.; et al. Electrochemical nature of the cathode interface for a solid-state lithium-ion battery: interface between $LiCoO_2$ and garnet-$Li_7La_3Zr_2O_{12}$. *Chem. Mater.* **2016**, *28*, 8051-9. DOI
57. Sun, W.; Shi, W.; Yang, J.; et al. Multi-element synergistic doping enhances high-voltage performance of $LiCoO_2$ via stabilizing internal and surface structures. *Electrochim. Acta.* **2024**, *504*, 144927. DOI
58. Jamil, S.; Yue, L.; Li, C.; et al. Significance of gallium doping for high Ni, low Co/Mn layered oxide cathode material. *Chem. Eng. J.* **2022**, *441*, 135821. DOI
59. Vardar, G.; Bowman, W. J.; Lu, Q.; et al. Structure, chemistry, and charge transfer resistance of the interface between $Li_7La_3Zr_2O_{12}$ electrolyte and $LiCoO_2$ cathode. *Chem. Mater.* **2018**, *30*, 6259-76. DOI
60. Bitzer, M.; Van, Gestel. T.; Uhlenbruck, S.; Hans-peter-buchkremer, . Sol-gel synthesis of thin solid $Li_7La_3Zr_2O_{12}$ electrolyte films for Li-ion batteries. *Thin. Solid. Films.* **2016**, *615*, 128-34. DOI

61. Rebohle, L.; Prucnal, S.; Skorupa, W. A review of thermal processing in the subsecond range: semiconductors and beyond. *Semicond. Sci. Technol.* **2016**, *31*, 103001. DOI

62. Ping, W.; Wang, C.; Wang, R.; et al. Printable, high-performance solid-state electrolyte films. *Sci. Adv.* **2020**, *6*, eabc8641. DOI PubMed PMC

63. Ramos, E.; Browar, A.; Roehling, J.; Ye, J. $CO_2$ laser sintering of garnet-type solid-state electrolytes. *ACS. Energy. Lett.* **2022**, *7*, 3392-400. DOI

64. Acord, K. A.; Dupuy, A. D.; Scipioni, Bertoli. U.; et al. Morphology, microstructure, and phase states in selective laser sintered lithium ion battery cathodes. *J. Mater. Proc. Technol.* **2021**, *288*, 116827. DOI

65. Zhu, H.; Liu, J. Emerging applications of spark plasma sintering in all solid-state lithium-ion batteries and beyond. *J. Power. Sources.* **2018**, *391*, 10-25. DOI

66. Li, L.; Andrews, J.; Mitchell, R.; Button, D.; Sinclair, D. C.; Reaney, I. M. Aqueous cold sintering of Li-based compounds. *ACS. Appl. Mater. Interfaces.* **2023**, *15*, 20228-39. DOI PubMed PMC

67. Waetzig, K.; Heubner, C.; Kusnezoff, M. Reduced sintering temperatures of $Li^+$ conductive $Li_{1.3}Al_{0.3}Ti_{1.7}(PO_4)_3$ ceramics. *Crystals* **2020**, *10*, 408. DOI